ELSEVIER SCIENTIFIC PUBLISHERS IRELAND

Computer Methods and Programs in Biomedicine 42 (1994) 167–180

computer methods and programs in biomedicine

A Monte Carlo program for the calculation of contrast, noise and absorbed dose in diagnostic radiology

Michael Sandborg*[a], David R. Dance[b], Jan Persliden[a], Gudrun Alm Carlsson[a]

[a]*Department of Radiation Physics, Faculty of Health Sciences, Linköping University, S-581 85 Linköping, Sweden*
[b]*Medical Physics Department, The Royal Marsden Hospital, Fulham Road, London SW3 6JJ, UK*

(Received 28 January 1993; revision received 13 October 1993; accepted 18 October 1993)

Abstract

A Monte Carlo computer program has been developed for the simulation of X-ray photon transport in diagnostic X-ray examinations. The simulation takes account of the incident photon energy spectrum and includes a phantom (representing the patient), an anti-scatter grid and an image receptor. The primary objective for developing the program was to study and optimise the design of anti-scatter grids. The program estimates image quality in terms of contrast and signal-to-noise ratio, and radiation risk in terms of mean absorbed dose in the patient. It therefore serves as a tool for the optimisation of the radiographic procedure. A description is given of the program and the variance-reduction techniques used. The computational method was validated by comparison with measurements and other Monte Carlo simulations.

Key words: Monte Carlo; Photon transport; Anti-scatter grid; Absorbed dose; Image quality; Optimisation

1. Introduction

Scattered radiation is a major problem in radiological imaging because it degrades contrast. In projection radiography its effects are reduced by the use of anti-scatter grids. A grid is constructed from a series of strips (normally lead) with a high X-ray absorption separated by interspaces with a low X-ray absorption. The grid geometry is designed to achieve a low transmission for secondary (scattered) photons, generated within the patient, but a high transmission for primary photons. It thus improves contrast but leads, in screen-film radiography, to higher absorbed doses in the patient. These effects are dependent upon the construction of the grid (geometry of the strips and interspaces) and the type of examination. The computational model described here was developed to study and optimise the design of grids for a wide range of X-ray examinations.

Monte Carlo methods are well established [1–15] for the study of imaging systems and dosimetry in diagnostic radiology. A review of their use in the radiological sciences and medical

* Corresponding author, Tel.: +46(13)224007; Fax: +46(13)224749.

SSDI 0169-2607(93)01439-Z

radiation physics have been given by Andreo [16]. Anti-scatter grids have been modelled by various authors [1–6].

Dance and Day [1] and Dance et al. [6] have calculated the influence of scatter and the performance of mammographic grids. Kalender [2,3] studied the distribution of scattered photons behind water slabs and evaluated the performance of different types of grid. Chan and Doi [4,12] made extensive Monte Carlo investigations of the characteristics of scattered radiation and the performance of grids in general radiology. Chan et al. [5] compared measurements and Monte Carlo calculations in order to validate their computational method. None of these authors, however, have discussed how to select the optimum grid for a particular imaging task.

The special features of the program described in this work are the ease by which the parameters can be varied and the simultaneous assessment of contrast (image quality) and patient dose. Also the positional variation of contrast in the image plane can be assessed with high resolution and precision. The program is thus an effective tool for the optimisation of the radiographic procedure [7,8].

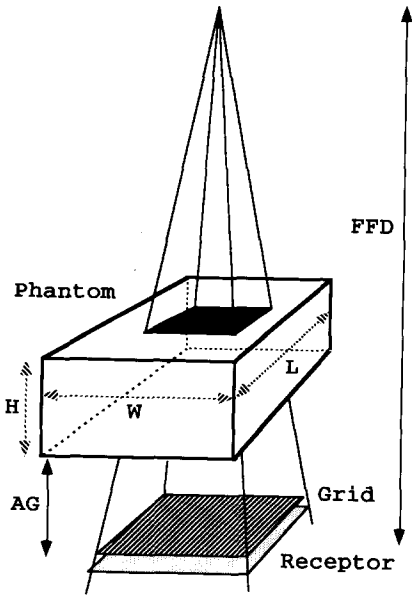

Fig. 1. The irradiation geometry showing phantom dimensions (length, L; width, W; thickness, H), the entrance field area (upper black area), air gap length, AG, and focus-receptor distance, FFD. The striped area shows the location of the grid, just above the image receptor.

2. Input data

The accuracy of Monte Carlo derived quantities depends directly on the choice of model input data. The calculations are repeatable only when detailed references are given to such data.

2.1. Irradiation geometry

Fig. 1 shows the geometric model which was used for the calculations. It comprises a rectangular slab of uniform composition which represents the patient, a grid and an image receptor. The slab was irradiated by a rectangular field defined by the collimation at the X-ray tube.

Different examination conditions were simulated by varying the size and orientation of the phantom, the beam entrance field, the focus-film distance and the positions of the grid and the image receptor. The phantom and the image receptor were separated by an air gap to allow for the grid and its movement mechanism. Many of the quantities calculated by the program are evaluated at a fixed point in the image receptor plane. This point may be freely chosen and is referred to as the 'point of interest'.

2.2. X-ray energy spectra

The X-ray photon energy spectra were calculated using a program developed by Birch et al. [17] and Birch (pers. commun., 1988). Data were available for an X-ray tube with a tungsten target, 3.0 mm aluminium total filtration and tube potentials between 30 and 150 kV. The data in each spectrum were tabulated at 1 keV intervals.

2.3. Photon interaction cross sections

The photo-electric cross-sections were taken from Berger and Hubbell [18], total and differential scattering cross sections from Hubbell et al [19] (incoherent scattering) and Hubbell and Øverbø [20] (coherent scattering), following the advice of Hubbell (pers. commun., 1991). The effect of inter-atomic binding on the scattering cross section [21] was neglected as no appropriate data ex-

ists for the materials we considered. Mass energy-absorption coefficients for air were taken from Hubbell [22].

The energies of the K-absorption edges in the image receptor were taken from Lederer and Shirley [23], as were fluorescent yields and intensities of K_α and K_β characteristic X-rays. The energies of the K_α and K_β characteristic photons and the probabilities of photo-electric interactions with K-shell electrons, were taken from Storm and Israel [24].

2.4. Phantom and contrasting detail

The phantom was modeled as a homogeneous block of soft tissue, or of tissue substitute material such as water or plexiglas (Fig. 1). It contained a thin, contrasting detail which served as a test-object for evaluating the contrast and signal-to-noise ratio (Section 3.1). The atomic composition of the contrasting detail was varied with the imaging situation and its thickness chosen so that a low but perceptible contrast was achieved.

2.5. Grids and air gaps

Fig. 2 shows the parameters used to specify the construction of the grid. Image quality and absorbed dose were also assessed without a grid so that scatter rejection associated with the use of an air gap could be investigated.

2.6. Image receptor

The receptors simulated were Kodak Lanex Regular screens (140 mg/cm^2 Gd_2O_2S), DuPont Par Speed screens (56 mg/cm^2 $CaWO_4$), DuPont Quanta II screens (85 mg/cm^2 BaFCl) and an image intensifier (100 mg/cm^2 CsI). The Quanta II screens are similar in composition and thickness to the standard plate used in the Fuji digital image plate system.

3. Quantities derived from Monte Carlo experiments

The energy imparted to the image receptor per unit area from primary, $\bar{\epsilon}_p$, and scattered photons, $\bar{\epsilon}_s$, and the energy imparted to the phantom, $\bar{\epsilon}$, can be combined to give information on image quality and mean absorbed dose in the phantom and grid performance. The bars on these three energy quantities show that they are the expectation values of stochastic variables. In this work estimates ϵ_p, ϵ_s and ϵ of these expectation values were calculated from individual Monte Carlo experiments. In each case the associated statistical error was estimated to ensure that adequate precision was achieved.

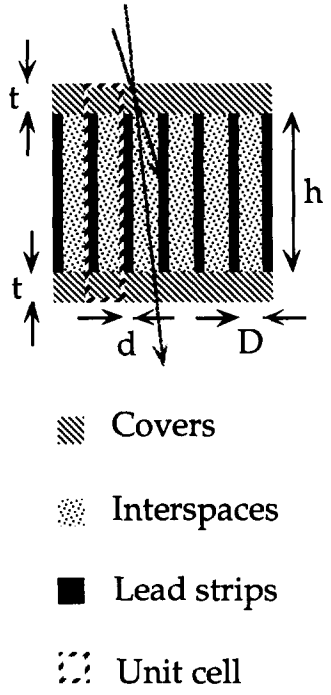

Fig. 2. Cross-section view of the central part of a grid. The focusing of the grid is not shown. The different areas show the components of the grid. The lead strip width is d, the interspace width is D, the interspace height is h, and the cover thickness is t. The grid ratio, $\mathbf{r}$, is defined by $\mathbf{r} = h/D$ and the strip density, N, by $N = (d + D)^{-1}$. The components of the unit cell (Section 4.5) are identified by the dashed rectangle. Two incident scattered photons are indicated by the dashed arrows; one passes through the grid and the other is absorbed in a lead strip.

3.1. Image quality descriptors

The image quality measures used were the contrast, C, and the signal-to-noise ratio, SNR. The contrast was calculated using [6]

$$C = \left(\frac{\epsilon_{p1} - \epsilon_{p2}}{\epsilon_{p1}}\right)(1 + \epsilon_s/\epsilon_{p1})^{-1} = C_p \cdot CDF \qquad (1)$$

where ϵ_{p1} and ϵ_{p2} are the energies imparted to the receptor by primary photons per unit area beside and behind the contrasting detail. The primary contrast, $C_p = (\epsilon_{p1} - \epsilon_{p2})/\epsilon_{p1}$, is obtained when only primary photons impart energy to the receptor. The contrast degradation factor, *CDF*, quantifies the loss of contrast due to scattered photons.

The signal-to-noise ratio, *SNR*, was calculated using [25]

$$SNR = \frac{|N_{p1} \cdot \lambda_{p1} - N_{p2} \cdot \lambda_{p2}|}{\sqrt{N_p \lambda_p^2 + N_s \lambda_s^2}} \qquad (2)$$

Here, N indicates the number of photons incident on an image element and λ is the energy imparted to the receptor by a single incident photon. Indices p and s stands for primary and in-phantom scattered photons, respectively, and indices 1 and 2 denote the image elements beside and behind the contrasting detail. The values of N and λ for the scattered photons are assumed to be the same for both image elements. Quantities of the form λ^2 are the second moments of the energy imparted to the receptor by a single incident photon. The contrasting detail was assumed to be thin enough that the modulation of the energy spectrum could be neglected in calculating the noise ($\lambda_{p1}^2 = \lambda_{p2}^2 = \lambda_p^2$ in the denominator of Eq. 2 [26,29]).

3.2. Dosimetric quantities

The energy imparted to the phantom was scored by summing the energy transfers to secondary electrons at each interaction within the photon transport. The mean absorbed dose in the phantom, D, was obtained by dividing the total energy imparted to the phantom by its mass and was used as a measure of radiation risk. Alm Carlsson and Carlsson [27] have shown that in a given projection, there is a fairly constant (beam quality independent) relationship between the mean absorbed dose in the body and radiation risk.

The entrance air collision kerma, $K_{c,air}$,

$$K_{c,air} = \int_0^{h\nu_{max}} h\nu \, \Phi_{h\nu}(h\nu) \, [\mu_{en}(h\nu)/\rho]_{air} \, d(h\nu) \qquad (3)$$

and the conversion factor between energy imparted to the phantom and air collision kerma integrated over beam area, $\epsilon/\int K_{c,air} dA$,

$$\frac{\epsilon}{\int_A K_{c,air} \, dA} = \frac{IF \cdot \overline{\cos\theta}}{\overline{(\mu_{en}/\rho)}_{air}} \qquad (4)$$

were also calculated. Here, $\Phi_{h\nu}(h\nu)$ is the number fluence of incident photons per unit energy interval and $(\mu_{en}/\rho)_{air}$ the mass energy absorption coefficient of air. The fraction, IF, of the incident energy, R_{in}, imparted to the phantom (the imparted fraction) was calculated from

$$IF = \frac{\epsilon}{R_{in}} \qquad (5)$$

In Eq. 4, $\overline{\cos\theta}$ and $\overline{(\mu_{en}/\rho)}_{air}$ are averages over the photons in the incident beam [28]. Eq. 4 is used for adapting measurements with a transmission ionisation chamber covering the beam area to mean absorbed dose in the patient.

Dosimetric quantities were normalised to a fixed value of the energy imparted to the receptor per unit area (film blackening) or to a fixed signal-to-noise ratio in the image receptor.

3.3. Quantities related to the performance of grids and air gaps

The contrast improvement factor due to the grid, *CIF*, was calculated from

$$CIF = \frac{C_{pg}}{C_p} \frac{1 + (\epsilon_s/\epsilon_p)}{1 + (\epsilon_s/\epsilon_p)_g} = \frac{C_{pg}}{C_p} \frac{CDF_g}{CDF} \qquad (6)$$

where the suffix g indicates that the grid is present and C_p and *CDF* are given in Eq. 1.

The dose increase factor, *DIF*, with a grid was calculated from

$$DIF = \frac{t_p}{t_{p,g}} \frac{1 + (\epsilon_s/\epsilon_p)}{1 + (\epsilon_s/\epsilon_p)_g} \qquad (7)$$

where t_p and $t_{p,g}$ are the fractional decreases in the energy imparted to the image receptor per unit

area by primary photons due to their attenuation in the phantom and in the phantom plus the grid, respectively. The DIF was calculated under the constraint of constant energy imparted per unit area to the receptor and corresponds to screen-film or image intensifier radiography.

The *SNR* improvement factor, *SIF*, was calculated from

$$SIF = \frac{SNR_g}{SNR} \tag{8}$$

where both *SNR* and SNR_g were estimated for fixed energy imparted to the receptor per unit area.

4. Program description

The computer program is based on programs developed by Dance and Day [1], Dance et al. [6], Dance [11], Persliden [13], Persliden and Alm Carlsson [14], and Sandborg and Alm Carlsson [29]. It uses the methods developed in these programs together with previously unpublished techniques for computation of quantities at points in the image plane and for the generation of secondary photons in the grid [10].

In this computer program, photon transport is simulated by tracing photons from the X-ray source through the soft tissue phantom, the grid and image receptor. By averaging over a large number (10^4–10^6) of photon histories, estimates of the energy imparted to the image receptor and to the phantom are made. As described in section 3, these estimates allow the derivation of contrast and signal-to-noise ratio and of the mean absorbed dose in the phantom. A flowchart of the main steps in the Monte Carlo program is given in Fig. 3.

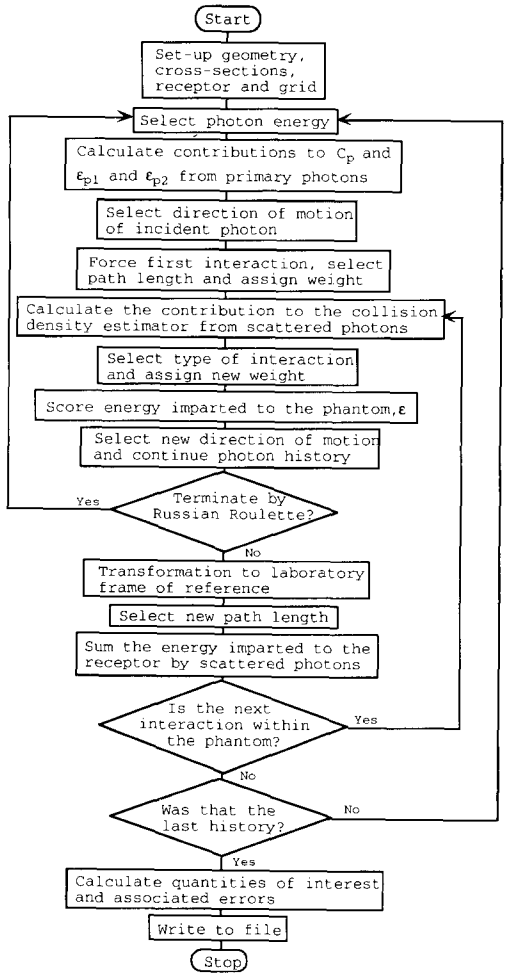

Fig. 3. Flow-chart of the main steps in the Monte Carlo program.

4.1. Selection of photon energy and initial direction of motion

Each photon simulated by the program started at the focal spot of the X-ray tube, and was directed towards the phantom within a collimated beam. The initial photon energy was selected using tabulated X-ray spectra and a modified rejection method [6] in which photons from the continuous bremsstrahlung spectrum and characteristic K-photons from the tungsten target were considered separately.

A laboratory frame of reference which was aligned with the phantom entrance surface was used (Fig. 4). The photon initial direction of motion (θ, ϕ) was selected assuming isotropic emission from the focal spot.

The polar angle, θ, was limited by the maximum angle allowed by the diagonal of the rectangular field [13], and the azimuthal angle was chosen randomly in the range 0–2π. Photon trajectories selected in this way, but lying outside the required rectangular field, were rejected.

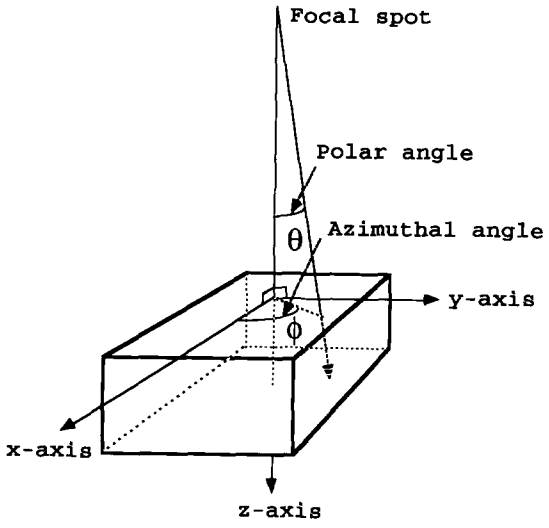

Fig. 4. The laboratory frame of reference fixed to the phantom, showing the x-, y- and z-axis, and the polar and azimuthal angles, θ and ϕ, before the first interaction.

4.2. Treatment of primary photons

In order to increase efficiency in calculating the difference in the energy imparted to the receptor beside and behind the contrasting detail (Eq. 1), analytic calculations and correlated sampling were used for primary photons. After each initial selection of photon energy, the energy imparted λ_p to the image receptor by a photon with this energy and directed towards the point of interest in the image plane, was calculated using Monte Carlo methods (Section 4.6.). The difference $(\epsilon_{1p} - \epsilon_{2p})$ in the energy imparted to the receptor beside (ϵ_{p1}) and behind (ϵ_{p2}) the contrasting detail was then calculated as $\epsilon_{p1} - \epsilon_{p2} = (t_1 - t_2)\lambda_p$, where t_1 and t_2 are the analytically calculated values of the photon transmission through the phantom (beside and through the contrasting detail, respectively) and the grid. The transmission through the grid was calculated using an analytic formula by Day and Dance [9].

4.3. Scattered photons generated within the phantom

Scattered photons arising from interactions in the phantom and reaching the receptor (image plane) were considered by means of the collision density estimator (Section 4.4). This estimator makes use of Monte Carlo generated photon histories in the phantom. Such histories were derived as described below. Photons started as described in Section 4.1 were followed into the phantom and allowed to interact. The first interaction in the phantom was forced. The bias which this procedure introduced was corrected for by assigning each photon an initial weight, w_1, given by

$$w_1 = 1 - e^{-[\mu(h\nu)H/\cos\theta]} \tag{9}$$

where $\mu(h\nu)$ is the linear attenuation coefficient for the phantom material, $h\nu$ the photon energy and H the thickness of the phantom. The path length, p, to the first interaction point was sampled from the truncated frequency function, using the distribution function method [13]

$$p = -\frac{1}{\mu(h\nu)} \log_e[1 - \rho(1 - e^{-[\mu(h\nu)H/\cos\theta]})] \tag{10}$$

where ρ is a random number in the interval (0,1). Subsequent interactions were not forced.

Photo-electric interactions do not contribute to the generation of scattered photons and such interactions were abandoned. All interactions were constrained to be coherent or incoherent scatterings. This method is called 'analytical averaging of survival' [30]. The bias introduced was corrected for by assigning a new weight, w_{n+1}, for the photon after its nth interaction, calculated from the cross sections for photo-electric, $\tau(h\nu_n)$, and scattering processes, $\sigma(h\nu_n)$:

$$w_{n+1} = w_n \frac{\sigma(h\nu_n)}{\tau(h\nu_n) + \sigma(h\nu_n)} \tag{11}$$

In this equation $h\nu_n$ is the energy of the photon before its nth interaction.

The scattering angle was selected, using the rejection method, from the sum of the differential cross sections for the coherent and incoherent scattering processes [1]. The azimuthal angle was selected uniformly in the range $0–2\pi$. The type of scattering (incoherent or coherent) was selected in

accordance with the relative magnitudes of the two differential scattering cross-sections. Atomic form factors and incoherent scattering functions were used to calculate these cross sections. This selection method was efficient because in low atomic number media the sum of the differential cross sections is not strongly peaked at any angle.

The scattering and azimuthal angles were derived in a coordinate system related to the direction of the photon before the interaction. The new photon direction in the laboratory frame of reference was calculated using a co-ordinate transformation [13]. The path length to the next interaction point was then selected and the photon history continued.

Either of two events could terminate a photon history. The first was when a photon was given a path length which took it outside the phantom. No scatter back to the phantom from the surrounding air or the grid was allowed. The second was when the history was artificially terminated because it had a low weight. In most cases the dimensions of the phantom were large compared to the mean free path of the photon, $1/\mu$. Many interactions would then be required to complete the photon history, and because of the decreasing weight w_n, the contributions to the collision density estimator would eventually become very small. To save computing time and increase the efficiency of the program, an unbiased technique known as 'Russian Roulette' [30] was used to terminate most histories once the weight fell below 0.05. Using this method a random number was selected, and in 95% of the cases the photon history was terminated; in 5% of the cases the photon history was continued with a statistical weight $w_{n+1} = 100\%/5\% = 20$ times the original one.

4.4. Collision density estimator

It was inefficient to use straight-forward Monte Carlo techniques to estimate the contribution from scattered photons at a specific point in the image plane. This was because of the low probability that a scattered photon would pass through a given small target area in the image receptor. The collision density estimator [14,31] was therefore used. Using this method, a contribution to the energy imparted per unit area is obtained from each interaction site of a photon history. This contribution was obtained in two steps. Firstly, the probability, T, per unit area (in the image plane) for the interacting photon to be scattered towards the point of interest, and to reach it without further interaction in the phantom or grid, was calculated analytically. Secondly, a photon with energy and direction corresponding to those for the probability calculation was traced into the receptor (Section 4.6) and a value λ_s was obtained for the energy imparted. Each photon history thus generated a contribution ϵ_s^* to the energy imparted to the receptor by scattered photons per unit area, given by

$$\epsilon_s^* = \sum_{n=1}^{N} W_n T(\alpha_n) \lambda_{n,s} \tag{12}$$

where $\lambda_{n,s}$ is the contribution from the n:th interaction site. The state vector α_n describes the photon's energy $h\nu_n$ and direction of motion Ω_n immediately prior to the nth interaction at $\mathbf{r}_n$.

$$\alpha_n = [\mathbf{r}_n, h\nu_n, \Omega_n, w_n] \tag{13}$$

Eq. 12 defines the collision density estimator. A detailed description of the calculations is given in the Appendix (including a contribution $\Delta\epsilon_s^*$ from secondary photons generated in the grid). The total energy imparted ϵ_s to the receptor per unit area was obtained by adding the contributions ϵ_s^* from each photon history.

4.5. Transmission of photons through the grid and generation of photons in the grid

The photons which reach the image receptor were divided into two sets; those (primary and scattered photons from the phantom) which passed the grid without any interaction, and secondary photons arising from interactions in the grid. The energy imparted to the image receptor by scattered photons in the first category was obtained from Eq. 12 using an analytical calculation of the grid transmission (t_{grid}) for a moving, focused grid according to the formula of Day and Dance [9]. The energy imparted to the receptor by photons in the second category (due to both primary and scat-

tered photons from the phantom) was estimated by straightforward Monte Carlo simulation of the passage of photons through the grid. For this purpose it was adequate to use a parallel grid with the same general parameters as the focused grid. In order to simplify the tracking of individual photon histories, the grid was treated as a series of unit cells, each consisting of a single lead strip and interspace with associated top and bottom covers (Fig. 2). Passage through the grid started at a randomly selected position (to simulate grid movement) on the upper surface of the unit cell (top of upper cover). The trajectory of each photon was followed until it left the unit cell or was absorbed. Photons leaving the unit cell through the upper surface and photons which were absorbed in the grid were given zero grid transmission. Photons leaving the unit cell through the lower surface, however, reach the image receptor and were given a transmission of 1. Photons leaving the unit cell at the side were considered as entering the same unit cell at the equivalent position on the other side and their histories within the grid were continued. Secondary photons (scattered photons or fluorescent K and L X-rays) generated within the grid and escaping into the receptor were traced in the receptor and the energy imparted scored. The K- and L-fluorescent X-rays arising from photoelectric interactions in the lead strips were generated in accord with the magnitudes of the relevant cross sections and fluorescent yields. This score was, for the scattered photons from the phantom, included in the collision-density based estimate (Eq. 12) with appropriate weighting (see Appendix).

It should be noted that the energy imparted to the receptor by secondary photons generated within the grid was calculated for photons initially directed towards the point of interest independent of the actual position at which their secondary photons entered the receptor. What we needed to calculate was the energy imparted by those secondary particles generated within the grid which crossed the target area. These two contributions to the energy imparted to the receptor are, however, approximately equal for a slowly varying fluence of photons incident on the grid because of the reciprocity of the two situations.

4.6. Energy imparted to the receptor

Many of the photons incident on the receptor pass through without interacting. To increase the efficiency of the program, the first interaction in the receptor was forced and the photon weight reduced in a similar way to Eq. 9. For the subsequent interactions, non-biased Monte Carlo transport was employed and photons were allowed to leave the receptor. Coherent and incoherent scattering and photo-electric interactions were simulated. Following a photo-electric interaction with energy above the K-edge of the receptor, there is a large probability for the emission of characteristic K-photons. Such photons were followed if their energy was higher than 10 keV. This was the case for elements with atomic number larger than 32. For elements with lower atomic number, K-photons were regarded to be locally absorbed and the photon history was terminated. The element within the receptor emitting the K-photon was chosen randomly according to the relative magnitudes of the appropriate photo-electric cross sections and atomic abundances. The energy of the K-photon was selected according to the emission probabilities of K_α and K_β X-rays. The choice of whether a K-photon or Auger electron was emitted was made according to the fluorescent yield. Characteristic L-photons were assumed to be locally absorbed since, for the elements considered, energies are less than 10 keV.

The energy imparted by an incident photon to the receptor was assumed to be contained within one voxel of the receptor (or pixel in the image). Any correlation between the energy impartation events in adjacent pixels was thus neglected. In screen-film radiography the fluorescent material is usually divided into two sheets separated by a film. The film was ignored here and the fluorescent material was treated as one sheet, which is adequate when only the energy absorption of the incident X-ray photons is considered. The limited dynamic range and spatial resolution of the image receptor were not simulated.

4.7. Error estimate in Monte Carlo derived quantities

The relative standard deviation, u, in the physical quantity, Q, was estimated as

$$\sqrt{\sum q^2 \Big/ \left(\sum q\right)^2}$$

The summations here are over all photon histories and the quantities q are the contributions to Q arising from each history.

5. Validation of the Monte Carlo program

To validate the program, the results were compared with measurements and other Monte Carlo calculations. Good agreement was obtained in all cases and the more important comparisons are given below.

5.1. Comparison measurements

5.1.1. Scatter-to-primary ratio with air gap. Calculations of the scatter-to-primary ratio, ϵ_s/ϵ_p (with air gap and without grid) were compared with measurements by Nielsen [32]. In the measurements a 30-cm air gap was used between a plexiglas slab and the image receptor. The field size was 30 × 30 cm^2 on the bottom of the slab and a 33 mg/cm^2 $CaWO_4$ receptor was used. Two situations were compared: 140 kV with a 10-cm plexiglas slab and 100 kV with a 20-cm slab. The precision in the measurements was ±4% (1 S.D.). Our calculations and Nielsen's measurements agree, within 2 S.D.

5.1.2. Grid transmission. Calculations of the primary and total grid transmissions, t_p and t_t, were compared with measurements by Chan et al. [5] in six situations. The field size was 30 × 30 cm^2 at the top of the phantom. The grid designs are described in Table 1, the thicknesses of the aluminium covers were 0.4 mm on each side and the interspace material was aluminium. A 1.3 cm air gap was used between the phantom and the grid. Our calculations agree, in 9 out of 12 tested cases, within two standard deviations of the measurements (Table 1). Differences between our Monte Carlo calculations and the measurements may be due to the fact that the calculations were performed on 'perfectly manufactured' grids whereas the measurements are made with real grids. Moreover, Chan et al. used a plexiglas tank with 1 cm thick walls filled with water whereas the simulations were made with water only. Plexiglas is known to generate more scattered photons than water [32]. The thickness of the aluminium covers of the experimental grids was not stated and this was an additional source of systematic uncertainty.

Comparisons with measurements by Walraven (J.P. Walraven (Smit Röntgen) pers. commun., 1991) were made for the transmitted primary fraction, t_p, the ratio between the contrast degradation factor with and without grid, CDF_g/CDF and the dose increase factor, *DIF* (Table 2). The measurements and the calculations were performed in the geometry suggested in IEC 627 [33].

Table 1
Comparison of primary and total grid transmission, t_p and t_t, derived from this work, with measurements by Chan et al. [5]

H[a] (cm)	U[b] (kV)	Recep.[c]	Grid *N/r/d*	t_p		t_t	
				This work	Chan et al. [5]	This work	Chan et al. [5]
25	70	LR	40/10/50	0.607 ± 0.004	0.621 ± 0.019	0.135 ± 0.008	0.127 ± 0.007
20	80	LR	40/8/50	0.645 ± 0.004	0.632 ± 0.019	0.203 ± 0.008	0.213 ± 0.012
20	80	PS	40/8/50	0.625 ± 0.003	0.633 ± 0.019	0.147 ± 0.008	0.151 ± 0.009
15	120	LR	40/10/50	0.649 ± 0.005	0.682 ± 0.020	0.241 ± 0.009	0.264 ± 0.015
20	80	LR	33/6/50	0.678 ± 0.006	0.682 ± 0.020	0.231 ± 0.009	0.257 ± 0.015
20	80	PS	40/15/50	0.543 ± 0.003	0.527 ± 0.016	0.094 ± 0.003	0.092 ± 0.005

The notation *N/r/d* means *N* strips/cm, grid ratio *r* and strip width *d* μm. The error range corresponds to 2 S.D.
[a]H denotes phantom thickness.
[b]U denotes tube potential.
[c]LR denotes Lanex Regular and PS denotes Par Speed image receptors.

Table 2
Comparison of Monte Carlo calculations (this work) and measurements by Walraven (pers. commun., 1991) of grid performance in the IEC 627 [33] geometry at 80 kV

Type of grid	DIF		CDF_g/CDF	
	This work	Walraven	This work	Walraven
SMIT/44/8/F/CF	4.09 ± 0.15	4.03 ± 0.24	3.23 ± 0.12	3.06 ± 0.18
SMIT/44/10/F/CF	4.88 ± 0.16	4.89 ± 0.29	3.80 ± 0.12	3.63 ± 0.22
SMIT/44/10/F/Al	5.43 ± 0.20	5.11 ± 0.31	3.85 ± 0.12	3.62 ± 0.22
LYSHOLM/40/8/Al/Al	5.15 ± 0.17	5.18 ± 0.31	3.48 ± 0.11	3.25 ± 0.20
LYSHOLM/40/10/Al/Al	6.12 ± 0.17	6.58 ± 0.39	3.96 ± 0.11	3.82 ± 0.23

The grids are specified in the form: manufacturer/strip density/grid ratio/interspace material/cover material. Cotton fibre is denoted F, carbon fibre CF and aluminium Al. The error range corresponds to 2 S.D. in the calculated values.

Grids of different designs and from different manufacturers were used. Our calculations agreed in 8 out of 10 cases within two standard deviations of the measurements by Walraven (pers. commun., 1991). The differences in the two remaining cases just exceeded two standard deviations. It has been reported [32] that the relative error in similar measurements was 6% (2 S.D.). Values of CDF_g/CDF were generally lower in the measurements, which may indicate that the grids were not manufactured perfectly.

5.2. Comparison with Monte Carlo calculations

5.2.1. Contrast degradation factors. Calculations of the contrast degradation factor, CDF, were compared with the work of Kalender [2]. The results are shown in Table 3 for five imaging configurations. In 4 out of 5 cases the two sets of calculations agreed within 2 S.D. Our values are slightly lower: partly because we calculated at a point in the field centre and Kalender in a small scoring area of 4 cm^2 around the centre and partly because different cross sectional data were used. The largest difference (7%) was found at 40 keV.

5.2.2. Fraction of energy imparted to the phantom. Calculations of the imparted fraction, *IF* (Eq. 5), were compared with the work of Alm Carlsson et al. [28], at various tube potentials, filtrations and phantom thicknesses. Values of the conversion factor between the energy imparted and air collision kerma integrated over beam area, $\epsilon/\int K_{c,air} dA$ (Eq. 4), were also compared. The two sets of results agreed within 2 S.D. in all cases.

5.2.3. Grid transmission. Comparison with Monte Carlo calculations by Chan et al. [5] was made for the transmitted primary fraction, the ratio between the contrast degradation factor with and without the grid, and the dose increase factor (Table 4). The calculations by Chan et al. [5] were for a pencil beam and an infinite scoring area which, by the principle of reciprocity, is equivalent to an infinite beam and a point scoring area. In our calculations, the phantom cross sectional area and

Table 3
Comparison of calculated contrast degradation factors, CDF, from this work with results from Kalender [2]

Field size (cm^2)	Photon energy (keV)	Contrast degradation factor (CDF)	
		This work	Kalender
10 × 10	60	0.629 ± 0.004	0.642 ± 0.015
20 × 20	40	0.458 ± 0.006	0.492 ± 0.020
20 × 20	60	0.471 ± 0.006	0.488 ± 0.020
20 × 20	120	0.532 ± 0.006	0.531 ± 0.019
30 × 30	60	0.424 ± 0.006	0.433 ± 0.023

Dimensions of water phantoms: thickness 10 cm, cross sectional area 30 × 30 cm^2. The focus receptor distance is 104 cm and the length of the air gap between the rear side of the phantom and the receptor (on the central axis) is 4 cm. The CDF is calculated in the field centre. The error range corresponds to 2 S.D.

Table 4
Comparison of t_p, CDF_g/CDF and DIF for different grid designs with Monte Carlo calculations by Chan et al. [5]

Grid *N/r/d*	t_p		*DIF*		CDF_g/CDF	
	This work	Chan et al. [5]	This work	Chan et al. [5]	This work	Chan et al. [5]
40/6/50	0.668 ± 0.003	0.665 ± 0.032	4.06 ± 0.22	4.07 ± 0.12	2.71 ± 0.15	2.71 ± 0.08
40/8/50	0.645 ± 0.003	0.637 ± 0.031	4.90 ± 0.26	4.92 ± 0.15	3.16 ± 0.17	3.13 ± 0.09
40/12/50	0.601 ± 0.003	0.597 ± 0.029	6.41 ± 0.41	6.36 ± 0.19	3.85 ± 0.24	3.79 ± 0.11
33/10/50	0.620 ± 0.003	0.617 ± 0.030	6.15 ± 0.39	5.77 ± 0.17	3.81 ± 0.24	3.56 ± 0.11
33/12/50	0.593 ± 0.003	0.585 ± 0.028	6.52 ± 0.29	6.48 ± 0.19	3.87 ± 0.17	3.79 ± 0.11
57/16/45	0.574 ± 0.003	0.594 ± 0.029	7.15 ± 0.42	6.74 ± 0.20	4.10 ± 0.24	4.00 ± 0.12

The image receptor is a Lanex Regular screen (140 mg/cm^2 Gd_2O_2S) and water slab thickness is 20 cm. The notation *N/r/d* means *N* strips/cm, grid ratio *r* and strip width *d* μm. The grids have aluminium covers and interspaces. The error range corresponds to 2 S.D.

field size were therefore chosen to be large (4 m^2 and 1 m^2, respectively), the focus-grid distance was 10 m and the scoring point positioned in the field centre (approximately simulating a broad parallel beam) with a 1.5-cm air gap between the phantom and the grid. The two sets of results agreed within 2 S.D. in 17 out of 18 tested cases. The difference in the remaining case just exceeded 2 S.D.

6. Application of the program

The program has been used in several applications. It was used to compare the performance of grids with different material (fibre or aluminium) for grid covers and interspaces [26]. A major application was the optimisation of grid design for a range of diagnostic procedures, where it was found that the choice of optimal parameters was dependent on phantom thickness [7,8]. Absolute values of the contrast and mean absorbed dose were calculated as a function of tube potential, and the grid parameters and tube potential found which gave a pre-defined level of image quality at the lowest dose.

7. Hardware and software specifications

The program was written in FORTRAN 77 and can run on VAX and SUN workstations. It uses 160 kb of memory including code and explanatory comments, and comprises 45 subroutines. The database of photon interaction cross sections, X-ray spectra, geometry, grid and image receptor specifications requires 300 kb of disk space shared between about 200 files. Each run produces a print-out of 15 kb containing relevant information from the simulation. The CPU-time per Monte Carlo experiment depends strongly on the operating parameters used and on the required statistical precision. A statistical precision of 3% in the scatter-to-primary ratio, requires $0.5–5 \cdot 10^5$ photon histories and 0.4–4.0 h of CPU-time on a VAX station 3100/30. The code was also implemented and run on a CRAY X-MP/48 and the CPU-time was then reduced by a factor of ten.

8. Program availability

The authors will be happy to consider running the program in any specific situation on request.

9. Conclusions

The Monte Carlo computational model described here is flexible and well defined in its set-up. The operating parameters (X-ray spectrum, irradiation geometry, grid and image receptor) can easily be varied to study individual effects or to survey different geometries and grid designs. When a large task is set out, such as guidance for the optimisation of image quality and radiation risk in diagnostic radiology, the Monte Carlo method is a convenient and flexible approach.

10. Acknowledgements

This work was supported by grants from the Commission of the European Communities Radiation Protection Program, (contract number Bi7-0019-C(CD) and F13P-CT92-0037) and from the Swedish National Institute of Radiation Protection (NIRP). We thank the senior scientists, Associate Professor E. Lund and Drs H.B.L. Pettersson and G. Matscheko, for constructive comments, particularly on 14 May, 1993.

11. Appendix: Use of the collision density estimator in calculating the energy imparted to the receptor per unit area by scattered photons

The collision density estimator was used to calculate the energy imparted to the receptor per unit area by scattered photons generated within the phantom. It allowed the calculation of this quantity at specified points in the image receptor plane so that the positional variation of image quality parameters could be derived with high spatial resolution and precision in a short computing time. The estimator was based on the simulated photon histories in the phantom (Section 4.3) and the energy imparted to the receptor was separated into contributions from (1) in-phantom scattered photons and (2) secondary photons generated by interactions in the grid.

A.1. The energy imparted to the receptor by photons transmitted through the grid

The energy imparted to the receptor per unit area at the point $\mathbf{r}_T$ in the image plane was calculated from Eq. 12. The probabilities $T(\alpha_n)$ were divided into contributions $T_{coh}(\alpha_n)$ and $T_{incoh}(\alpha_n)$ arising from coherent and incoherent scatterings, respectively, which were calculated using

$$T_{coh}(\alpha_n) = \frac{1}{\mu(h\nu_n)} \frac{d\sigma_{coh}}{d\Omega_T} \frac{\cos(\Omega_T, \mathbf{e}_z)}{|\mathbf{r}_T - \mathbf{r}_n|^2} e^{-\mu(h\nu_n)d} t_{grid}(h\nu_n, \Omega_T) \quad (A.1)$$

$$T_{incoh}(\alpha_n) = \frac{1}{\mu(h\nu_n)} \frac{d\sigma_{incoh}}{d\Omega_T} \frac{\cos(\Omega_T, \mathbf{e}_z)}{|\mathbf{r}_T - \mathbf{r}_n|^2} e^{-\mu(h\nu_{Comp})d} t_{grid}(h\nu_{Comp}, \Omega_T) \quad (A.2)$$

where $\mu(h\nu)$ is the linear attenuation coefficient for the phantom material for a photon of energy $h\nu$, $d\sigma_{coh}/d\Omega_T$ and $d\sigma_{incoh}/d\Omega_T$ are the linear differential scattering cross sections per unit solid angle. The photon directions before and after the scatter are Ω_n and $\Omega_T = (\mathbf{r}_T - \mathbf{r}_n)/|\mathbf{r}_T - \mathbf{r}_n|$, respectively. The length, d, is the distance between $\mathbf{r}_n$ and the boundary of the phantom in the direction Ω_T, and $t_{grid}(h\nu,\Omega_T)$ is the probability that a photon of energy $h\nu$ and direction of motion Ω_T will be transmitted through the grid without interaction. The vector, $\mathbf{e}_z$, is perpendicular to the surface of the receptor. The quantity $h\nu_{Comp}$ is the energy of the photon after a Compton scatter towards $\mathbf{r}_T$. Energy broadening of the photon energy due to the motion of bound electrons was neglected [34]. For each interaction point $\mathbf{r}_n$ in the photon history, the energies imparted to the receptor $\lambda_{n,s}$ (Section 4.6) for photons incident at $\mathbf{r}_T$ with direction of motion Ω_T and with energies $h\nu_n$ and $h\nu_{Comp}$ were calculated. The unbiased estimate ϵ_s^* was then calculated using

$$\epsilon_s^* = \sum_{n=1}^{N} w_n [T_{coh}(\alpha_n)\lambda_{n,s}(h\nu_n, \Omega_T) + T_{incoh}(\alpha_n)\,\lambda_{n,s}(h\nu_{Comp}, \Omega_T)] \quad (A.3)$$

A.2. The energy imparted to the receptor by secondary photons generated within the grid

The contribution, $\Delta\epsilon_s^*$, to the energy imparted to the receptor per unit area at the point $\mathbf{r}_T$ due to secondary photons generated within the grid was estimated using

$$\Delta\epsilon_s^* = \sum_{n=1}^{N} w_n [P_{coh}(\alpha_n)\epsilon_{rec.\,sc}(h\nu_n, \Omega_T) + P_{incoh}(\alpha_n)\,\epsilon_{rec.\,sc}(h\nu_{Comp}, \Omega_T)] \quad (A.4)$$

Here, the $P(\alpha_n)$ are of the form $T(\alpha_n)/t_{grid}(h\nu,\Omega_T)$ and correspond to the probability of a photon being scattered from $\mathbf{r}_n$ towards the point $\mathbf{r}_T$ and reaching the upper surface of the grid without interacting in the phantom. The energies imparted $\epsilon_{rec,sc}(h\nu,\Omega_T)$ were derived as follows: a photon with direction of motion Ω_T, energy $h\nu$, and moving towards $\mathbf{r}_T$, was traced through the grid (Section 4.5). Any secondary photons generated in the grid and reaching the receptor were followed to the receptor (Section 4.6) and the energy imparted scored.

Contrary to the scores, $\lambda_{n,s}$ in Eq. (A.3), the scores $\epsilon_{rec,sc}$ in Eq. (A.4) took values of zero with high probability. Since incident photons were forced to interact in the receptor (Section 4.6) a zero score in Eq. (A.3) would be obtained only if the incident photon escaped the receptor after one or more coherent scatterings.

For each photon trajectory in the phantom, the contribution to the total energy imparted to the receptor per unit area by scattered photons was finally obtained as the sum of $\epsilon_s^* + \Delta\epsilon_s^*$ of the contributions in eqs. (A.3) and (A.4).

A contribution $\Delta\epsilon_s^*$ to ϵ_s from primary photons interacting in the grid was calculated and added in a similar manner taking into account the probability of an incident primary photon to be transmitted to the upper surface of the grid without interacting in the phantom.

12. References

[1] D.R. Dance and G.J. Day, The computation of scatter in mammography by Monte Carlo methods, Phys. Med. Biol. 29 (1984) 237–247.

[2] W.A. Kalender, Monte Carlo calculations of x-ray scatter data for diagnostic radiology, Phys. Med. Biol. 26 (1981) 835–849.

[3] W.A. Kalender, Calculation of X-ray grid characteristics by Monte Carlo methods, Phys. Med. Biol. 27 (1982) 353–361.

[4] H.-P. Chan and K. Doi, Investigation of anti-scatter grids: Monte Carlo simulation studies, Phys. Med. Biol. 27 (1982) 785–803.

[5] H.-P. Chan, Y. Higashida and K. Doi, Performance of anti-scatter grids in diagnostic radiology: Experimental measurements and Monte Carlo simulation studies, Med. Phys. 12 (1985) 449–454.

[6] D.R. Dance, J. Persliden and G. Alm Carlsson, Calculation of dose and contrast for two mammographic grids, Phys. Med. Biol. 37 (1992) 235–248.

[7] M. Sandborg, D.R. Dance, G. Alm Carlsson and J. Persliden, Monte Carlo study of grid performance in diagnostic radiology: factors which affect the selection of tube potential and grid ratio, Br. J. Radiol. 66 (1993) 1164–1176.

[8] M. Sandborg, D.R. Dance, G. Alm Carlsson and J. Persliden, Monte Carlo study of grid performance in diagnostic radiology: task dependent optimisation for screen-film imaging, Br. J. Radiol. 67 (1994) 76–85.

[9] G.J. Day and D.R. Dance, X-ray transmission formula for anti-scatter grids, Phys. Med. Biol. 28 (1983) 1429–1433.

[10] G.J. Day and D.R. Dance, A method for simulating the generation of secondary photons within anti-scatter grids (unpublished) (1981).

[11] D.R. Dance, The Monte Carlo calculation of integral radiation dose in xeromammography, Phys. Med. Biol. 25 (1980) 25–37

[12] H.-P. Chan and K. Doi, Physical characteristics of scattered radiation in diagnostic radiology: Monte Carlo simulation studies, Med. Phys. 12 (1985) 152–165.

[13] J. Persliden, A Monte Carlo program for photon transport using analogue sampling of scattering angle in coherent and incoherent scattering processes, Comput. Methods Programs Biomed. 17 (1983) 115–128.

[14] J. Persliden and G. Alm Carlsson, Calculation of the small-angle distribution of scattered photons in diagnostic radiology using a Monte Carlo collision density estimator, Med. Phys. 13 (1986) 19–24.

[15] R.L. Morin (editor), Monte Carlo simulation in the Radiological Sciences (CRC Press, Boca Raton, FL., 1988).

[16] P. Andreo, Monte Carlo techniques in medical radiation physics (review), Phys. Med. Biol. 36 (1991) 861–920.

[17] R. Birch, B. Marshall and G.M. Ardran, Catalogue of spectral data for diagnostic X-rays, The Hospital Physicists' Assoc., Scientific Rep. Ser. 30 (47 Belgrave Square London, 1979).

[18] M.J. Berger and J.H. Hubbell, XCOM: Photon cross section on a personal computer, NBSIR 87-3597, U.S. Dep. of Commerce, Natl. Bureau of Standards, Office of Standard Reference Data (Gaithersburg MD 20899, U.S.A., 1987).

[19] J.H. Hubbell, Wm.J. Veigele, E.A. Briggs, R.T. Brown, D.T. Cromer and R.J. Howerton, Atomic form factors, incoherent scattering functions and photon scattering cross sections, J. Phys. Chem. Ref. Data 4 (1975) 471–538.

[20] J.H. Hubbell and I. Øverbø, Relativistic atomic form factors and photon coherent scattering cross sections, J. Phys. Chem. Ref. Data 8 (1979) 69–105.

[21] L.R.M. Morin, Molecular form factors and photon scattering cross sections of water, J. Phys. Chem. Ref. Data 11 (1982) 1091–1098.

[22] J.H. Hubbell, Photon mass attenuation and energy-absorption coefficients from 1 keV to 20 MeV, Int. J. Appl. Radiat. Isot. 33 (1982) 1269–1290.

[23] C.M. Lederer and V.S. Shirley, Eds., Table of isotopes, Seventh edition (Wiley & Sons, New York, 1978).

[24] E. Storm and H.I. Israel, Photon cross sections from 1 keV to 100 MeV for elements Z = 1 to Z = 100, Nuclear Data Tables A7 565–688 (Academic Press, New York, 1970).

[25] A.M. Kellerer, Mikrodosimetrie, Grundlagen einer theorie der strahlenqualitet p.78 (Munich: Gesellschaft für Strahlenforschung).

[26] M. Sandborg, D.R. Dance, G. Alm Carlsson and J. Persliden, Selection of anti-scatter grids for different imaging tasks: the advantage of low atomic number cover and interspace materials. Br. J. Radiol. 66 (1993) 1151–1163.

[27] G. Alm Carlsson and C.A. Carlsson, Relations between the effective dose equivalent and mean absorbed dose (energy imparted) to patients in diagnostic radiology, Phys. Med. Biol. 31 (1986) 911–921.

[28] G. Alm Carlsson, C.A. Carlsson and J. Persliden, Energy imparted to the patient in diagnostic radiology: calculation of conversion factors for determining the energy imparted from measurements of the air collision kerma integrated over beam area, Phys. Med. Biol. 29 (1984) 1329–1341.

[29] M. Sandborg and G. Alm Carlsson, Influence of energy spectrum, contrasting detail and detector on the signal-to-noise ratio (SNR) and detective quantum efficiency (DQE) in projection radiography, Phys. Med. Biol. 37 (1992) 1245–1263.

[30] G. Alm Carlsson, Effective use of Monte Carlo methods for simulating photon transport with special reference to slab penetration problems in X-ray diagnostics, ULi-RAD-R-49 Rep. Ser. ISSN 0348-7679 (Dep. of Radiat. Phys., Linköping Univ., Sweden, 1981).

[31] U. Fano, L.V. Spencer and M.J. Berger, Penetration and diffusion of X-rays, in: Flügge, Ed., Encyclopaedia of Physics, Neutrons and related gamma ray problems, XXXVIII/2 660–817 (Springer-Verlag, Berlin, 1959).

[32] B. Nielsen, Scattered radiation in diagnostic radiology. Measurements, reduction and influence on image quality, in: Thesis (Univ. of Linköping ISBN 91-7372-781-4, Sweden, 1985).

[33] International Electrotechnical Commission, IEC Standard, Characteristics of anti-scatter grids used in X-ray equipment, Publication 627 (Geneva Suisse first edition, 1978).

[34] G. Alm Carlsson, C.A. Carlsson, K.F. Berggren and R. Ribberfors, Calculation of scattering cross sections for increased accuracy in diagnostic radiology, I. Energy broadening of Compton-scattered photons, Med. Phys. 9 (1982) 868–879.